Enhanced pervaporative performance of hybrid membrane by incorporating amphiphilic carbonaceous material

Boxin Gao [a,b], Zhongyi Jiang [a,b], Guanhua Liu [a,b], Ruisi Xing [a,b], Hong Wu [a,b], Fusheng Pan [a,b,*], Baoyi Wang [c], Xingzhong Cao [c]

[a] Key Laboratory for Green Chemical Technology of Ministry of Education, School of Chemical Engineering and Technology, Tianjin University, Tianjin 300072, China
[b] Collaborative Innovation Center of Chemical Science and Engineering (Tianjin), Tianjin 300072, China
[c] Key Laboratory of Nuclear Analysis Techniques, Institute of High Energy Physics, Chinese Academy of Sciences, Beijing 100049, China

ABSTRACT

Amphiphilic carbonaceous material (ACM) was blended with sodium alginate (SA) and then deposited onto the polyacrylonitrile (PAN) porous support layer to fabricate SA-ACM/PAN hybrid membranes. As a two-dimensional material, ACM provided anisotropy, horizontal stacking orientation and high aspect ratio. The abundant oxygen-containing functional groups ($-NO_2$, $-SO_3H$, $-OH$, $-COOH$ and epoxy group) on the edge of ACM (proved by X-ray photoelectron spectroscopy and scanning electron microscope with energy dispersive X-ray (EDX) spectrometer) offered the hydrophilic region, while the unoxidized part on the surface of ACM offered hydrophobic region. The hydrophilic region on ACM could preferentially adsorb water molecules and then facilitate water molecules entering the transport channel due to the hydrogen bond, while the hydrophobic region could realize the fast diffusion of water molecules. The small nanosheet size (200–400 nm, observed by atomic force microscopy) could interfere the arrangement of polymer chains more efficiently. The hybrid membranes exhibited the optimal permeation flux of 1778 g/m^2 h and separation factor of 1816 for ethanol dehydration under 76 °C and 10 wt% feed water concentration, which is much higher than that of SA membrane (increased by 139% and 306%, respectively).

© 2016 Elsevier B.V. All rights reserved.

1. Introduction

Dimensionality plays an essential role in influencing their fundamental properties, in addition to the composition and arrangement of atoms in materials [1]. Two-dimensional (2D) materials provide a vast and diverse untapped source of layered substance with anisotropy, horizontal stacking orientation and high aspect ratio, which are essential for separation, sensing, catalysis and energy storage applications [2]. Novoselov et al. established a convenient method to prepare a variety of free-standing atomic 2D crystals (especially graphene) by using micromechanical cleavage in 2004, which has made the application of 2D materials in diverse fields a research hotpot [3]. Among those fields, polymer-inorganic hybrid membrane by incorporating 2D materials into the polymer to enhance the separation performance

has received tremendous attention [4–7]. In the hybrid membranes, 2D materials prefer to accept the configuration parallel to the membrane surface, which can improve interfacial interactions between polymer-inorganic interfaces more effectively to optimize the structure and property of hybrid membrane [8–11]. The space between stacking layers of 2D materials could form the molecule transport channels, which is beneficial for the separation performance [12]. Meanwhile, the processability and flexibility of polymer could offset the defects generated from the accumulation of 2D materials [13]. Polymer-2D inorganic material hybrid membranes have achieved extensive application in separation performance, due to it can combine the advantages of polymer and 2D inorganic material.

2D materials used for the preparation of polymer-inorganic hybrid membrane mainly include molecular sieve, zeolite, metal organic framework (MOF) and graphene oxide (GO). Among various 2D materials, GO, usually coming from flake graphite, has been widely used due to its special properties, such as high specific surface area (2600 m^2/g), single atomic layer and handy surface modification [14]. It has been proved that both the functional

---

* Corresponding author at: Key Laboratory for Green Chemical Technology of Ministry of Education, School of Chemical Engineering and Technology, Tianjin University, Tianjin 300072, China.
E-mail address: fspan@tju.edu.cn (F. Pan).

groups and size of GO nanosheets have a significant influence on the performance of the polymer-GO hybrid membranes. Compared with graphene, GO with plenty of oxygen-containing groups including hydroxyl, carboxyl and epoxy groups are beneficial for dehydration separation in membranes [15]. Zhao et al. introduced additional oxygen-containing groups, such as $-SO_3H$, onto GO by grafting zwitterionic PSBMA. The PSBMA@GO nanosheets enhanced the hydrophilicity of the sodium alginate (SA) membrane by hydrogen bonds to endow the high-efficiency water permeation [16]. Meanwhile, the small nanosheet size can provide more edge-to-edge slits as penetration paths for water, which construct molecular-sieving channels and structural pores to enhance the separation performance more efficiently [17]. Chen et al. prepared GO membranes consisting of small GO sheets (lateral size of 200–400 nm) for the dehydration of butanol. Benefited from removing the larger GO sheets (lateral size of 4–6 μm), the membrane exhibited better separation performance [18]. Therefore, it can be envisaged that if a novel 2D material is synthesized with more oxygen-containing groups (especially more hydrophilic groups) and smaller size, the performance of the fabricated polymer-inorganic hybrid membranes will be further enhanced.

Amphiphilic carbonaceous material (ACM), as another typical 2D GO-like material, was firstly synthesized by Fujii et al. [19–22]. Besides the typical 2D characters, ACM nanosheets are amphiphilic: the region connected with oxygen-containing functional groups is hydrophilic, while the unoxidized region is hydrophobic. The abundant oxygen-containing groups attached on the nanosheets of ACM mainly contain $-NO_2$, $-SO_3H$, $-OH$, $-COOH$ and epoxy group [23]. The hydrophilicity of $-NO_2$ and $-SO_3H$ is stronger than that of $-COOH$ and $-OH$, due to their larger electronegativity providing stronger ability to attract electron and form hydrogen bonds with water molecules. Due to the introduction of oxygen-containing groups ($-NO_2$, $-SO_3H$) with larger volume, the distance between ACM layers is large enough to make the material dispersing steadily in water [24]. Meanwhile, the small nanosheet size (200–400 nm) could enhance the interaction between inorganic filler and polymer to interfere the arrangement of polymer chains more efficiently [25]. Last but not least, the raw material of ACM is green needle coke, refined from petroleum residual oil. By means of the mixed acid process, no organic solvent is used in the preparation of ACM [24]. This can realize the recycling of the industry trash, in order to save resources and protect the environment. It is rare to find the applications of ACM nanosheets in fabricating hybrid membrane in the existing researches.

In this study, the ACM was blended with SA and deposited onto polyacrylonitrile (PAN) ultrafiltration membranes to prepare the hybrid membranes. Due to the hydrophilic property, SA polymer had been widely used as membrane material in pervaporation dehydration [26]. The physical morphology, chemical structure and thermal stability of both the ACM nanosheets as well as the SA-ACM hybrid membranes were characterized. The pervaporation dehydration performance of the hybrid membranes was evaluated using ethanol-water mixtures. The effects of ACM content, operation temperature and feed concentration on the membrane separation performance were investigated, and the long-term operation stability was also evaluated.

2. Experiment

2.1. Materials

Green needle coke (NC) was supplied by Jinzhou Petrochemical Co. Ltd. (Jinzhou, China). Sodium alginate (SA) was supplied by Qingdao Bright Moon seaweed Group Co. Ltd. (Shandong, China).

Calcium chloride dihydrate ($CaCl_2 \cdot 2H_2O$), absolute ethanol and silver nitrate ($AgNO_3$) were bought from Tianjin Guangfu Technology Development Co. Ltd. (Tianjin, China). Concentrated sulfuric acid (H_2SO_4, 98 wt%), concentrated nitric acid (HNO_3), hydrochloric acid (HCl) and sodium hydroxide (NaOH) were gained from Tianjin Kewei Ltd. (Tianjin, China). Polyacrylonitrile (PAN) ultrafiltration membranes used as membrane substrates with a molecular weight cut-off of 100 kDa were obtained from Shanghai Mega Vision Membrane Engineering & Technology Co. Ltd. (Shanghai, China).

All the reagents were of analytical grade and used without further purification. Deionized water through a Millipore system (MillisQ) was used in all experiments.

2.2. Membrane preparation

2.2.1. Preparation of ACM nanosheets

ACM was prepared from green needle coke with high carbon content, low volatile and ash content, by the mixed acid process. NC of 20–50 μm prepared by crushing and sieving was blended uniformly with a mixture of concentrated nitric acid and sulfuric acid. The reaction was terminated by putting the reactant into cold distilled water. The mixture was washed with distilled water until the filtrate was neutral. The solid collected from the mixture was mixed with NaOH solution (pH > 12) and stirred to dissolve at 80 °C. Then hydrochloric acid was added to the filtrate (pH < 1.8). ACM was washed by distilled water and gained after stoving [27].

2.2.2. Fabrication of SA-ACM hybrid membranes

The hybrid membranes were fabricated by spin-coating membrane casting solutions blending with SA polymer and ACM nanosheets onto PAN ultrafiltration membranes. The PAN ultrafiltration membranes soaked in deionized water were cut into sizes of 0.1 m × 0.1 m, then hung up and dried at room temperature for 3 h for preparation to serve as support layers. In a typical procedure, an appropriate amount of SA polymer was dissolved in deionized water stirring at 30 °C for 1 h. Certain amounts of ACM nanosheets were dispersed in aqueous solution by ultrasonic vibration (achieved by Noise Isolating Tamber SCIENTZ-IID) for 5 min. The solution was dropwise added into the SA solution and stirred vigorously for another 5 h. After filtration and deaeration by gauze, the membrane casting solution was spin-coated onto PAN substrates, with the spin coating at 500 rpm for 25 s then 800 rpm for 40 s using WS-400BZ-6NPP/LITE spin coater. The hybrid membranes were placed at room temperature for 24 h to evaporate the solvent. After immersed in 0.5 M $CaCl_2$ solution for 10 min and rinsed with abundant water, the cross-linked membranes were obtained.

For simplicity, the hybrid membranes were designated as SA-ACM-X/PAN, where X represented the content of ACM in SA (wt%). The X varied from 1 to 3 for SA-ACM-X/PAN. For characterization and swelling study, the corresponding homogeneous membranes were fabricated on glass plates instead of PAN substrates following a similar preparation procedure and denoted as SA-ACM-X.

2.3. Characterizations

The morphology of the ACM nanosheets was determined by transmission electron microscopy (TEM, JEOL JEM-100CXII) and atomic force microscopy (AFM, CSPM5000). The apparent and cross-section morphologies of the ACM nanosheets and hybrid membranes were measured using field emission scanning electron microscope (FESEM, Hitachi S-4800, Japan), while the category and distribution of atoms on the ACM surface were probed in combination with energy dispersive X-ray (EDX) spectrometer (SEM/EDX).

The chemical structure of the ACM was measured using Raman spectra (2400–350 cm^{-1}, DXR Smart Raman Spectrometer-Thermo Fisher Scientific Co, USA, with an excitation source of Nd:YAG laser 532 nm). The chemical properties of ACM and hybrid membranes were performed by FTIR spectra (Nicolet-560 Fourier transform infrared spectrometer with a scan range of 4000–500 cm^{-1} and resolution of 1.93 cm^{-1}). The chemical compositions of ACM were analyzed by X-ray photoelectron spectroscopy (XPS, Kratos Axis Ultra DLD with a monochromatic Al Kα source and charge neutralizer) and elemental analysis (Elementar, Vario Micro cube). The crystallization properties of ACM and membranes were investigated by X-ray powder diffraction (XRD, D/MAX-2500 X-ray diffractometer, CuKα, 40 kV, 200 mA) with a range of 3–70° and speed of 3 °C/min at room temperature. Thermogravimetric analysis (TGA) of ACM nanosheets and membranes was determined by a thermogravimetric analyzer (NETZSCH-TG209 F3). The phase transition behavior of the hybrid membranes was measured by a Pyris Diamond differential scanning calorimetry (DSC, Netzsch 204 F1). About 10 mg of membrane samples were cut into small pieces, heating from room temperature to 150 °C for 0.5h, then cooling to 0°C to eliminate the influence of the adsorbed water in the membranes. Then the samples were heated from 0 to 170 °C at a rate of 10 °C /min with nitrogen protection.

The free volume property of membrane was observed by positron annihilation lifetime spectroscopy (PALS) measurements using an EG&G ORTEC fast-slow coincidence system with a resolution of 209 ps. The positron source (^{22}Na, 13 μci) was sandwiched between two pieces of samples with a size of 1 cm × 1 cm and thickness of approximately 0.5 mm. The assumed model of the free volume was a spherical potential surrounded by an electron layer with thickness Δr, which accepted 0.1656 nm as an estimated value. The apparent fractional free volume (f_{app}) of membranes could be calculated by the following semiempirical equations, which revealed the correlation between o-Ps annihilation lifetime (τ_3) and radius of the free volume cavity (r_3) [28].

$$\tau_3 = \frac{1}{2}\left[1 - \frac{r_3}{r_3 + \Delta r} + \left(\frac{1}{2\pi}\right)\sin\left(\frac{2\pi r_3}{r_3 + \Delta r}\right)\right]^{-1}$$
(1)

$$f_{app} = \frac{4\pi}{3}r_3^3 I_3$$
(2)

Mechanical stability of the membranes was obtained by an electronic stretching machine (Xinke WDW 3020) at a strain rate of 5 mm/min. The membrane surface hydrophilicity was measured by static contact angle meter (JC2000C). By dropping water droplets onto at least 10 different sites of each membrane surface, an average value was acquired. Swelling degree (SD) was gained by weighing the homogenous membranes dried in vacuum oven (W_D). To achieve sorption equilibrium, the samples were submerged in 90 wt% ethanol aqueous solution under 350 K for 48 h and weighed after quickly removing the surface liquid (W_S). The SD value was determined from this equation

$$SD = \frac{W_S - W_D}{W_D} \times 100$$
(3)

2.4. Pervaporation experiments

Pervaporation for removal of water from the organic solvent is an important membrane process. In this study, pervaporation experiments were performed on the P-28 membrane module (CM-Celfa AG Company, Switzerland) with an effective membrane area of 37.38 cm^2. The temperature of feed solution (90 wt% ethanol-water) was kept at 349 K by a thermal bath and the vacuum on the permeate side was maintained below 0.1 kPa by a vacuum pump.

The retentate was recycled back to the feed tank with a flow rate of feed solution kept at 60 L/h. The permeate vapor was condensed in liquid nitrogen cold traps at 30 min intervals after reaching steady state. HP4890 gas chromatograph was employed to analyze the composition of collected samples and feed solution. The permeation flux (J, g/m^2 h) and separation factor (α) were estimated from equations below to assess the separation performance

$$J = \frac{Q}{A \times t}$$
(4)

$$\alpha = \frac{P_W/P_E}{F_W/F_E}$$
(5)

where Q was the weight (g) of permeate collected during a time interval t (h) and A was the effective membrane area (m^2); P and F represented the mass fractions of water (W) and ethanol (E) in both permeate and feed solutions, respectively. Take reliability and accuracy as considered, each experiment was repeated by three duplicated membrane samples fabricated under the same condition, and each sample was tested for three times. The testing results of all nine measurements were averaged as the final data and deviations were shown as error bars to determine the separation performance parameters. The permeance (($P/l)_i$ GPU, where 1 GPU = 7.501 × 10^{-12} m^3 (STP)/m^2 s Pa), and selectivity (β) were calculated from [29].

$$(P/l)_i = \frac{J_i}{p_{io} - p_{il}} = \frac{J_i}{\gamma_{io}\chi_{io}p_{io}^{sat} - p_{il}}$$
(6)

$$\beta = \frac{(P/l)_W}{(P/l)_E}$$
(7)

where J_i was the permeation flux of component i (g/m^2 h), l was the membrane thickness (m), P_{io} and P_{il} were the partial pressures (kPa) in the feed side and permeate side, respectively. P_{il} could be considered as approximately zero, due to the high vacuum in the permeate side. γ_{io} and χ_{io} were the activity coefficient and mole fraction in the liquid feed, respectively, and p_{i0}^{sat} was the saturated vapor pressure (kPa) of the pure component. The permeation flux of every component was transformed into volumes under standard temperature and pressure (STP): 1 kg of water vapor at STP = 1.245 m^3 (STP); 1 kg of ethanol vapor at STP = 0.487 m^3 (STP) [30]. The detailed description of pervaporation measurements could be found in our previous work [31].

3. Results and discussion

3.1. Characterization of ACM

The morphology of ACM was characterized by TEM and AFM. The TEM image in Fig. 1(a) clearly showed that ACM had 2D morphology and nanosheet structure with a number of wrinkles and grooves. The lateral size of ACM nanosheets was approximately 200–400 nm, which was generally smaller than GO (The horizontal sizes of GO in different references were listed in Table S1). The lateral dimension and nanosheet thickness of ACM were also observed by AFM. Fig. 1(b) further showed the small lateral size of ACM nanosheets and Fig. 1(c) revealed the thickness of ACM nanosheets was approximately 14 nm from the height profile.

The distribution of elements on the ACM nanosheet surface was explored by SEM/EDX images. Fig. 2(a) exhibited the SEM image of ACM nanosheets, while Fig. 2(b)–(e) illustrated the distribution of carbon, oxygen, sulfur and nitrogen atoms on the
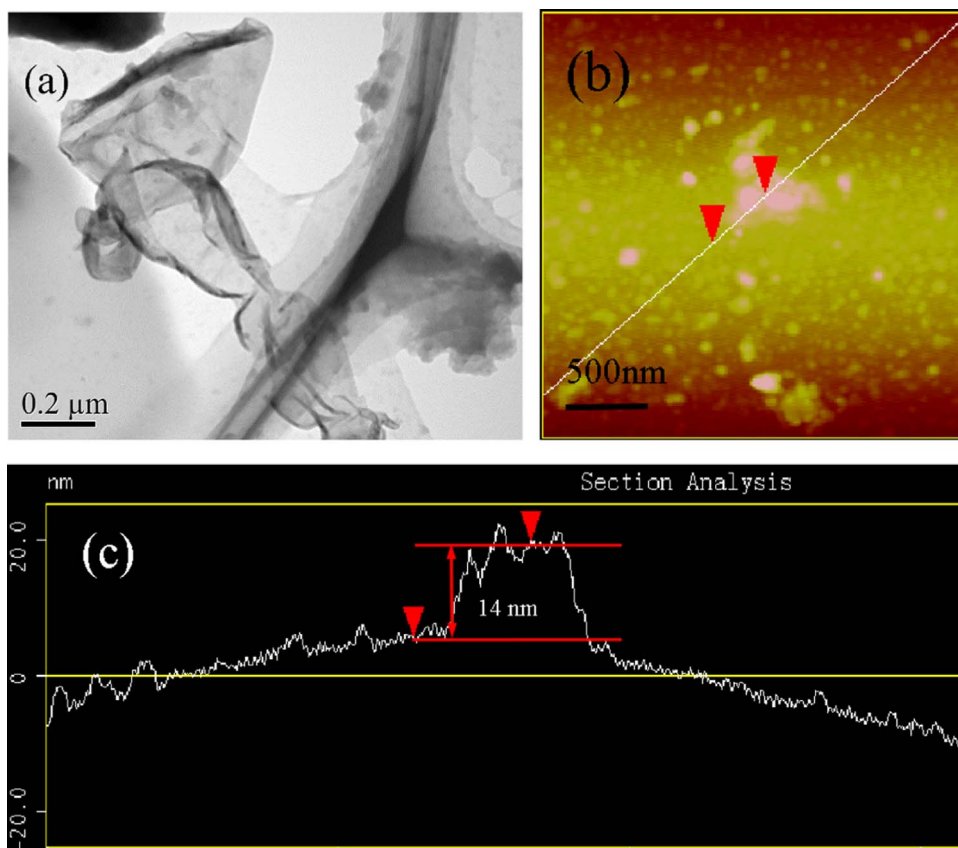
Fig. 1. (a) TEM and (b) (c) AFM images of ACM.

nanosheet surface, respectively. According to the SEM/EDX analyses, these elements were dispersed throughout the ACM nanosheets and the distributions of S, O and N at the edge were higher than that at the center.

Raman spectroscopy was used to acquire the structural message and oxidation extent of ACM. Fig. 3(a) showed that both the ACM and its homogeneous membranes had two characteristic bands. D band (1346 cm^{-1}) represented cavities and grain boundaries of ACM caused by the oxidation process from needle coke [32]. G band (1615 cm^{-1}) referred to the non-oxide region, which had the carbon framework of sp^2 hybridization [33]. The intensity ratio of D band to G band (I_D/I_G) of ACM was 0.97, which was higher than GO ($I_D/I_G=0.94$), indicating that ACM had higher oxidation extent than GO [34].

Characteristic peaks of functional groups in ACM were observed by the FT-IR spectra shown in Fig. 3(b). The peaks at 1235, 1723, 1298, 1625 and 3482 cm^{-1} were attributed to the C–O, H–O stretching vibration, C=O symmetrical stretching vibration of carboxyl group, C–O–C stretching vibration of epoxy group, C=C stretching vibration of aromatic ring and H–O stretching vibration of hydroxyl group, respectively. Other than these common chemical bonds, the peaks at 1357, 1534 cm^{-1} (symmetrical and asymmetrical stretching vibration of NO$_2$) and 1039, 1087 cm^{-1} (symmetrical stretching vibration of SO$_2$) were the unique oxygen-containing groups of ACM nanosheets. The oxygen-containing functional groups of ACM nanosheets were generally more abundant than GO. Fig. 3(b) also exhibited that, when ACM was blended into the SA matrix, the characteristic peaks of functional groups occurred blue shift for approximately 210 cm^{-1}. This was due to the carboxyl and hydroxyl functional groups of SA could form strong hydrogen bonds with oxygen-containing groups of ACM.

The zeta potential analysis of ACM dispersed in deionized water (0.05 wt%) was −38.07 mV, which represented sufficient mutual repulsion to ensure dispersion stability [35]. The oxygenic groups connected with the edges of ACM could give the nanosheets negative charge after ionization, which led to electrostatic repulsion among nanosheets to maintain favorable dispersity in water and remained steady for approximately 7 days [19,20,27,36].

More detailed elemental composition and chemical bonds information of ACM were further revealed by XPS. The percentage composition of elements in ACM was C 72.60%, O 25.65%, S 1.75%, respectively. The low C/O ratio of 2.83 shown Fig. 4(a) indicated a high oxidation degree [37,38]. The high-resolution C 1s spectra of ACM in Fig. 4(b) could be divided into three peaks at binding energies of 284.6, 286.0 and 287.4 eV, which were attributed to C–C/C=C (48.72%), C–O/C–O–C (38.40%) and O–C=O (12.89%), respectively [39]. The high proportion of hydroxyl C (C–O), epoxy C (C–O–C) and carboxylate C (O–C=O) revealed that ACM possessed large accounts of oxygen-containing groups. The elemental analysis demonstrated N element occupied 3.49%.

3.2. Characterization of membranes

3.2.1. Morphology of hybrid membranes

The cross-section morphologies were characterized by FESEM and shown in Fig. 5. Fig. 5(a)–(b) exhibited the active layers with thickness approximately 300 nm were deposited firmly on the PAN support layer. Fig. 5(c)–(h) showed that compared with the smooth cross-section of pure SA homogeneous membrane, the configuration of ACM in hybrid membrane gradually turned into brick-and-mortar architectures [40], along with the filling content increased. The ACM nanosheets exhibited horizontal stacking orientation. The surface SEM images in Fig. S1 showed that the hybrid membrane surface was as smooth as the pure membrane. It was hard to observe nanosheets on the surface due to the low content of ACM.
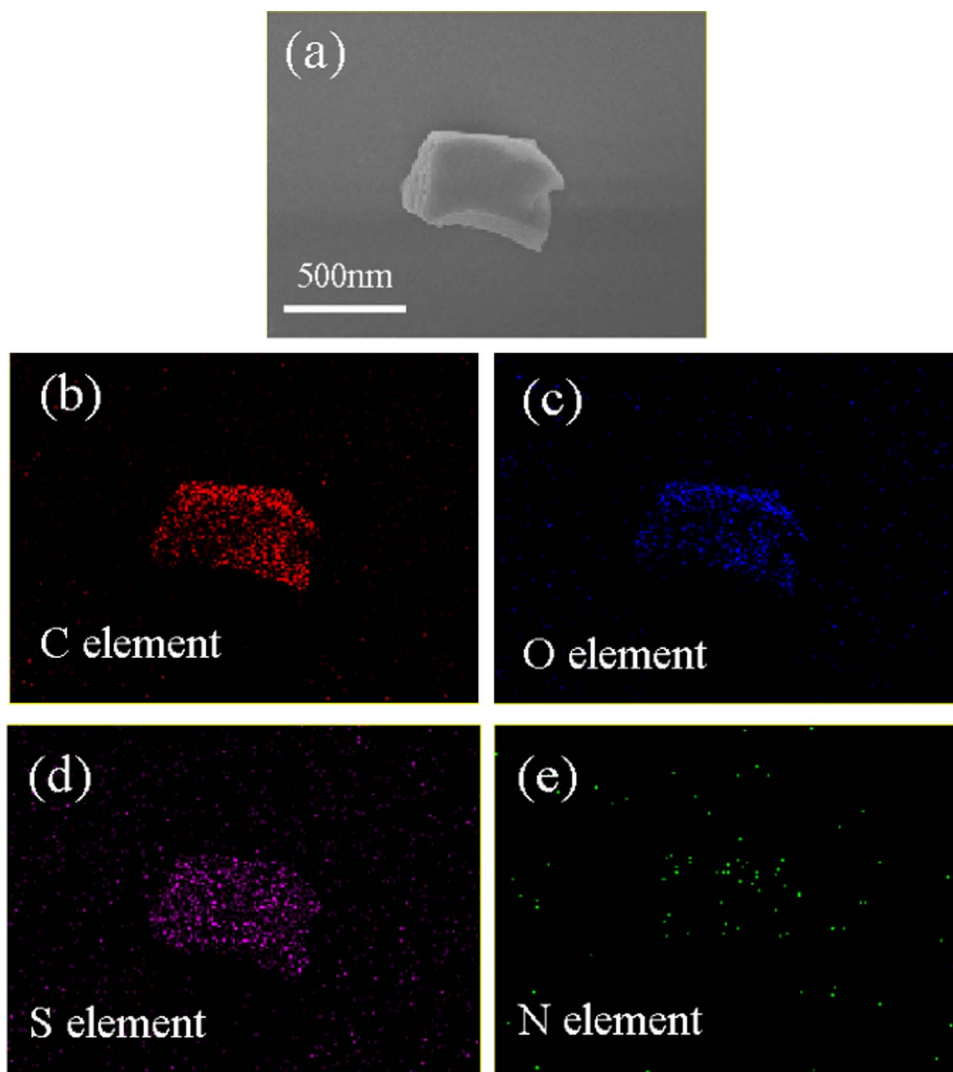
Fig. 2. (a) SEM image of the ACM nanosheet and (b-e) EDX mappings of carbon, oxygen, sulfur and nitrogen atoms on the ACM nanosheet, respectively.

3.2.2. Crystallinity of membranes

The XRD patterns of ACM in Fig. 6 showed the (002) and (100) diffraction peaks at $2\theta=26°$ and $44°$, respectively. The XRD patterns of hybrid membranes exhibited only the typical diffraction peak of SA ($2\theta=22.6$), while none characteristic peak of ACM ($2\theta=26°$, $44°$) was observed. It indicated that ACM nanosheets were dispersed in polymer matrix homogeneously. Polymer crystallinity had a significant influence on the mass transfer process. Higher crystallinity of polymer matrix led to diffusion paths of penetrant molecules more tortuous [41]. The trend of diffraction peak intensity in hybrid membranes decreased at first (1.5, 2 wt%) and then increased (2.5, 3 wt%) as the ACM content increased. The effect of ACM content on diffraction peak intensity of hybrid membranes was shown in Fig. S2. When the filling content of ACM was low, the inorganic nanosheets could disturb the arrangement of polymer, induce more amorphous regions and enlarge the inter-chain distance [42]. Therefore, the crystallinity declined when the content of ACM increased at first. As the filling content became higher, the slight aggregation of nanosheets weakened its ability to disturb the arrangement of the polymer. Meanwhile, SA chains on the surface of nanosheets were induced to be ordered arranged by 2D ACM nanosheet, acting as nucleating agent, which led to the rise of crystallinity.

3.2.3. Free volume property of hybrid membranes

The free volume property of membranes listed in Table 1 was assessed by PALS characterization. Accompanied by the increasing ACM content, the fractional free volume of hybrid membranes increased firstly and then decreased, which were all higher than pure SA membrane. At the same content of 2D material, smaller nanosheet size would provide higher specific surface and offer more diffusion paths for molecule transport, which formed more free volume cavities in the SA-ACM interfaces and increased the fractional free volume. Meanwhile, more oxygen-containing groups of ACM could provide stronger interfacial interaction between polymer and inorganic filler to avoid the non-selective defects at the interface, which was beneficial to form free volume cavities to enhance the selectively of membranes. In this study, as the content increased, the number and radius of free volume cavities in the interfaces increased slightly. When the content of ACM was 2 wt%, the hybrid membrane had largest free volume radius (0.251 nm). As the ACM content increased continuously, the re-stacking of ACM nanosheets led to the decrease of fractional free volume. The larger radius was beneficial for molecule transport, which could enhance the permeability of the hybrid membrane.

3.2.4. Hydrophilicity

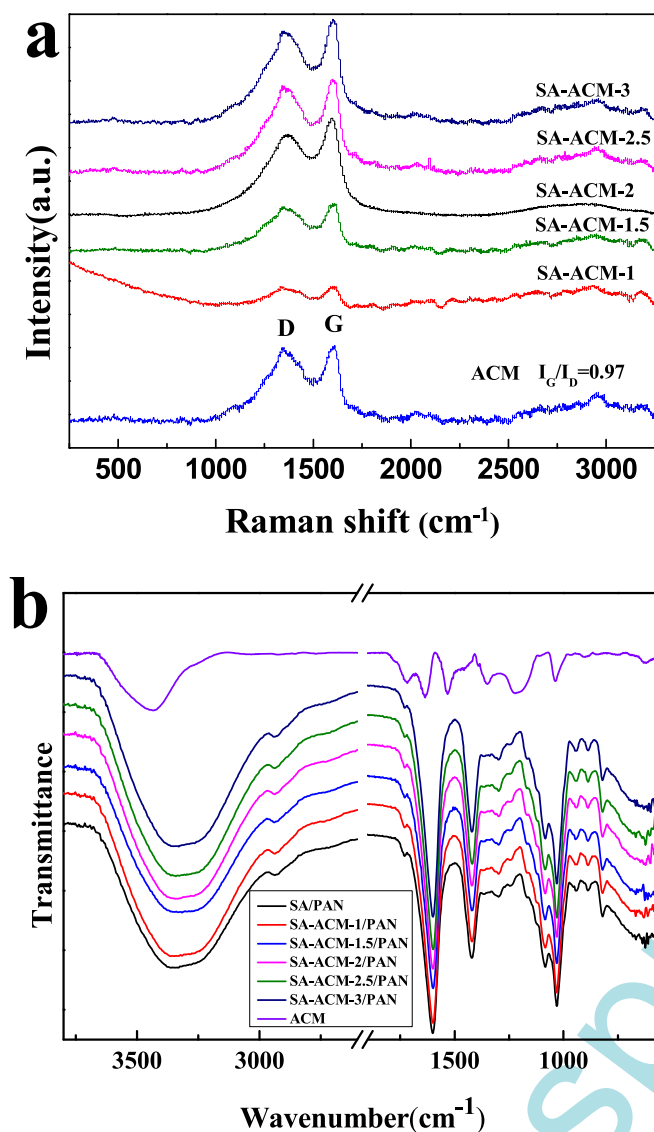As shown in Table 2, the contact angles of water on the surface

Fig. 3. (a) Raman and (b) FT-IR spectra of ACM.

Fig. 4. (a) XPS wide-scan spectra and (b) high-resolution C 1s spectra of ACM.

of SA-ACM/PAN membranes were measured to evaluate the hydrophilicity. On account of most ACM nanosheets were embedded in the SA matrix, which had a slight influence on the hydrophilicity of hybrid membrane surface, contact angles mainly maintained at approximately 38°, similar to the SA pure membrane. To research the stability of membranes, swelling experiment were conducted. Table 2 exhibited that the swelling degrees of hybrid membranes decreased accompanied by the increasing ACM content. All the hybrid membranes exhibited lower swelling degree than SA pure membrane. This was because the strong interface interaction between SA polymer and ACM filler restricted the stretching of the SA chains in aqueous solution and enhanced the swelling resistance of membranes.

3.2.5. Thermal properties analysis

Thermal stability of the ACM nanosheets and SA-ACM homogeneous membranes was evaluated by TGA under nitrogen atmosphere. Fig. 7(a) demonstrated that the decomposition process of the hybrid membranes involved three stages, as the reference [9,43] described. The vapor evaporation below 200 °C in the first stage corresponding to the traces of moisture mainly contained the weight loss of free water and bound water in SA polymer and ACM nanosheet. The decomposition of oxygen-containing
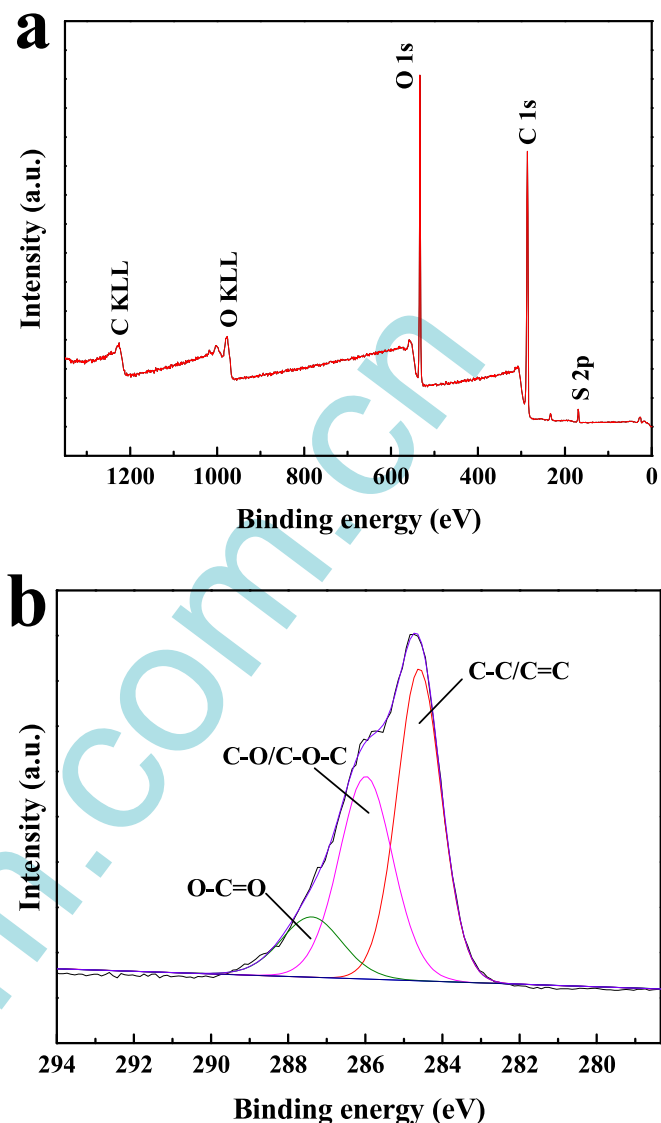
functional groups in SA and ACM, such as –NO$_2$, –SO$_3$H, –OH, –COOH and epoxy group, mainly occurred in the second stage between 200 and 400 °C. And the pyrolysis of SA polymer chains appeared in the third stage in the range of 400–600 °C, which resulted in the degradation of SA backbone. The thermal stability was evaluated by the first stage of decomposition temperature, which was approximately 205 °C to all the membranes and 260 °C to ACM nanosheets. These results indicated that ACM nanosheets displayed a better thermostability than SA matrix. The ACM-filled membranes exhibited almost similar thermal stabilities and thermal decomposition behaviors to SA pure membrane. Such temperatures were much higher than the typical operation temperature (around 70 °C), which ensured the thermal stabilities of membranes.

Glass transition temperature (Tg) could be used to investigate the mobility of the polymer chains. The DSC curves of SA-ACM and SA pure membranes were shown in Fig. 7(b), respectively. Tgs of all the SA-ACM membranes were lower than the SA pure membrane. As the content of ACM increased, Tg of hybrid membrane declined first and then increased. These results illustrated that ACM was dispersed well at low content, which could interfere the order packing of polymer in the crystalline region to enhance the mobility. The interfacial interaction sites did not increase
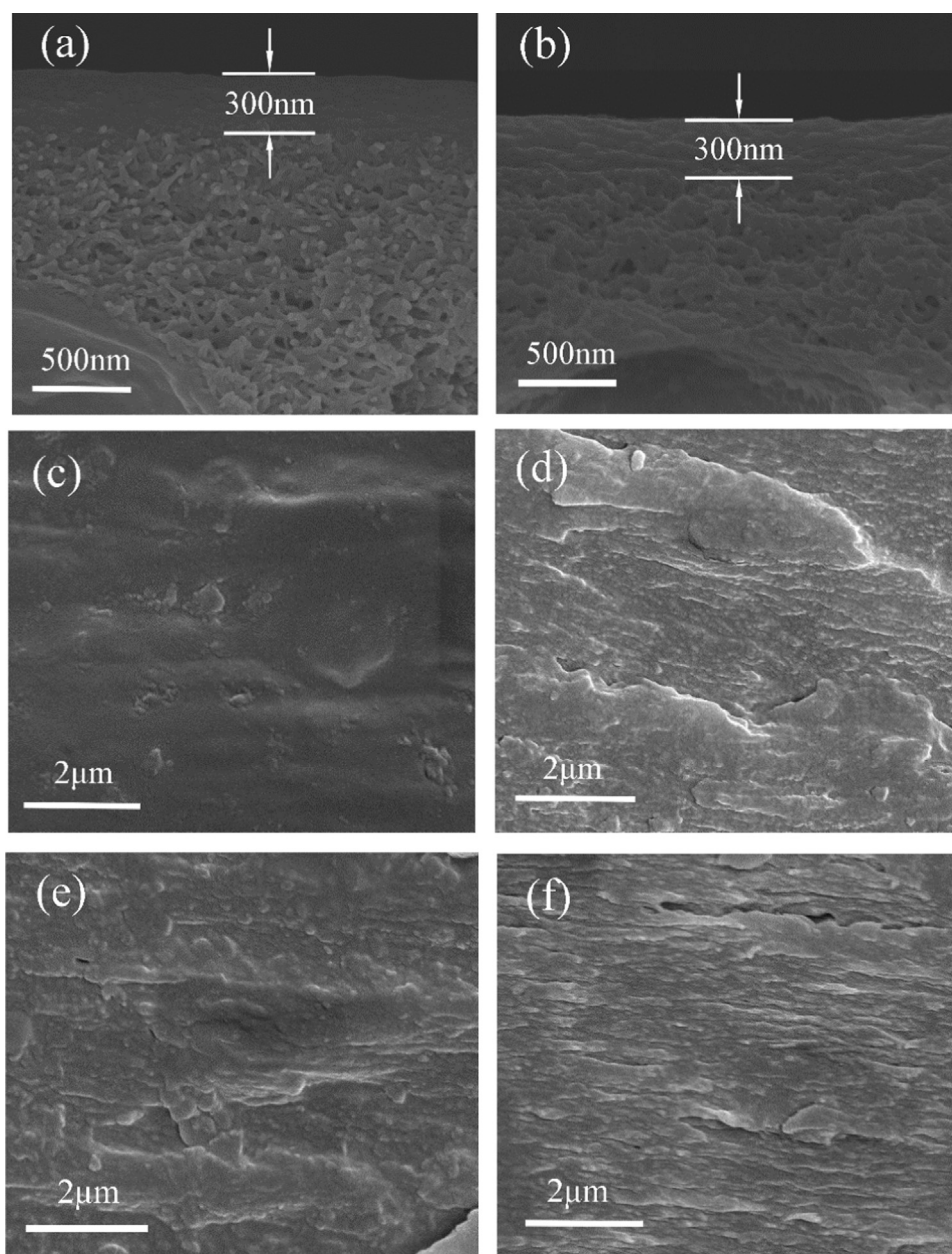
Fig. 5. SEM images of the cross-section of (a) SA/PAN, (b) SA-ACM-2/PAN, (c) SA pure, (d) SA-ACM-1, (e) SA-ACM-2 and (f) SA-ACM-3.

proportionally to the content of ACM at higher ACM content in the hybrid membranes because of the agglomeration of nanosheets, which weakened the influence of nanosheets on polymer chains mobility.

3.2.6. Mechanical property of hybrid membrane

The tensile strength and tensile modulus of homogeneous membranes listed in Table 3 were significantly enhanced compared to SA pure membrane when ACM was added. The brick-and-mortar formation and interfacial interaction enhanced the structural strength and declined the flexibility of SA chains. The tensile strength and tensile modulus of SA-ACM-2 increased by 31.76% and 111.83%, respectively. By the influence of nanosheet agglomeration, the tensile strength and tensile modulus of SA-ACM-2.5 and SA-ACM-3 declined gradually.

4. Pervaporation performance of the membranes

4.1. Effect of ACM content

In order to investigate the influence of ACM content on membrane separation performance, pervaporation experiments of hybrid membranes were conducted with 90 wt% ethanol aqueous solution at 350 K. Fig. 8 showed the separation factor and permeation flux of the SA-ACM/PAN. Accompanied with the increase of ACM content, both the separation factor and permeation flux first increased and then decreased. When the content of the ACM increased from 0 to 2 wt%, the permeation flux increased from 1279 to 1778 g/m^2 h and the separation factor also increased from 594 to 1816.

The transport of penetrant molecules through SA-ACM hybrid membrane was proposed and schematically diagramed in Fig. 9. The adsorption-diffusion process was profited from amphiphilicity of ACM nanosheets. Each oxygen-containing functional group at
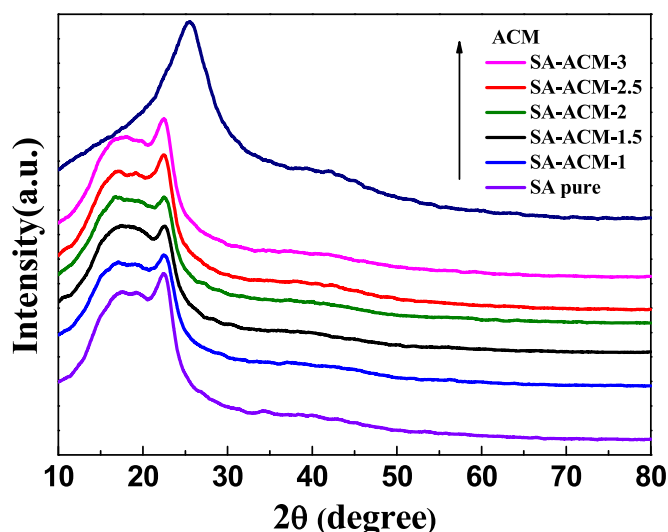
Fig. 6. XRD patterns of ACM, SA pure, SA-ACM-X.

Table 1
Free volume property of pure SA and SA-ACM-X homogeneous membranes.

Membrane	$I3$ (%)	$\tau3$ (ns)	$r3$ (nm)	f_{app}
Pure SA	8.09 ± 0.27	1.613 ± 0.020	0.246 ± 0.002	0.507 ± 0.030
SA-ACM-1	8.56 ± 0.29	1.576 ± 0.016	0.242 ± 0.002	0.510 ± 0.028
SA-ACM-2	8.02 ± 0.28	1.652 ± 0.023	0.251 ± 0.002	0.529 ± 0.034
SA-ACM-3	8.19 ± 0.30	1.617 ± 0.020	0.247 ± 0.002	0.516 ± 0.032

Table 2
Water contact angle and swelling degree of different membranes.

ACM content (wt%)	Water contact angle (°) SA-ACM-X/PAN	Swelling degree (%) SA-ACM-X
0	39 ± 2	7.04 ± 0.50
1	39 ± 3	6.63 ± 0.46
1.5	38 ± 2	6.32 ± 0.48
2	38 ± 2	6.14 ± 0.50
2.5	40 ± 3	5.72 ± 0.50
3	39 ± 2	5.41 ± 0.48

Fig. 7. (a) TGA and (b) DSC curves of SA pure, SA-ACM-X.

Table 3
Mechanical property of membranes.

ACM content (wt%)	Strength of extension (MPa)	Elasticity modulus (GPa)
0	85	3.38
1	105	4.13
1.5	106	5.58
2	112	7.16
2.5	107	6.99
3	105	6.16

the edge of ACM nanosheets acted as a hydrophilic kernel. Water molecules were adsorbed preferentially to these hydrophilic kernels by hydrogen bonds and then penetrated into the interval between the ACM nanosheets. The pressure in the downstream side actuated water molecules diffused rapidly through the un-oxidized region to the next hydrophilic kernel, due to its low friction contact with the hydrophobic carbon framework. While the smaller polarity of ethanol molecules gave it higher friction resistance, which led to the difference between water and ethanol in transport rate. The oxygen-containing functional groups dispersed throughout the ACM nanosheets and their distributions at the nanosheet edge were higher than at the center (shown in Fig. 2), which indicated the hydrophilicity of the nanosheet edge was higher than the center. Therefore, the adsorption and diffusion process took the leading role at the nanosheet edge and center, respectively. By means of repeating this process, water transport channels were formed, which realized preferential appeal and fast transport of water molecules in the membrane. The interplanar distance corresponding to the crystallographic plane (002) of ACM was 0.36 nm, which was between the kinetic diameter of water (0.26 nm) and ethanol molecules (0.45 nm). The proper distance between stacking layers could sieve water and ethanol molecules in some extent. The transport efficiency and
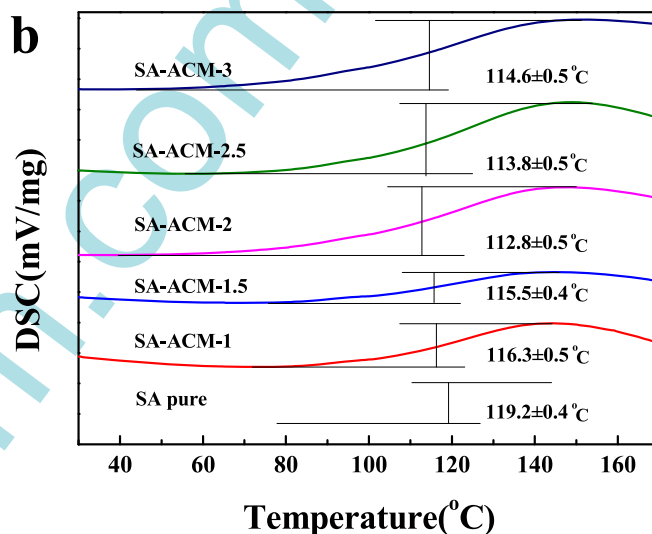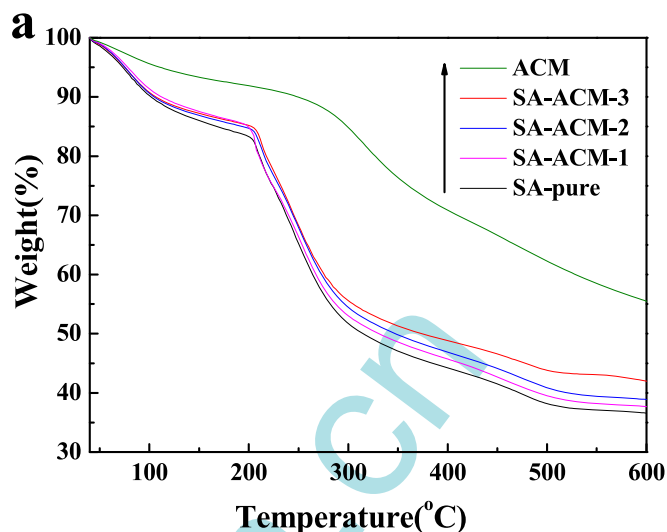
speed of ethanol molecules were lower than water molecules, which enhanced the selectivity. Meanwhile, the small nanosheet size of ACM could enhance the interaction between inorganic filler and polymer and decrease inter-chain interaction, which enlarged the inter-chain distance more efficiently. Small nanosheet size could also reduce the crystallinity of ACM and increase the fractional free volume to enhance permeation flu [44]. Therefore, benefited from the amphiphilicity and small size of ACM nanosheets, SA-ACM hybrid membrane exhibited higher permeability and selectivity.

The performances of pervaporation dehydration with hybrid membranes containing 2D material from literature were shown in Table 4 in comparison to the results of this investigation. It can be
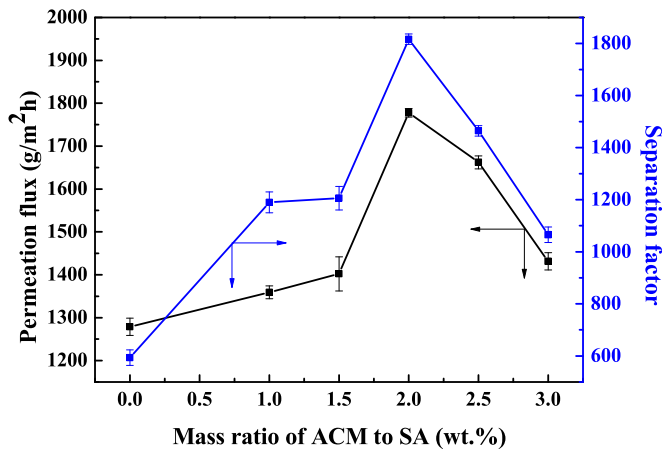
Fig. 8. Pervaporation performance of SA pure/PAN and SA-ACM-X/PAN.

seen that the membranes in this study exhibited higher permeation flux and selectivity, which were an important feature for industrial application.

4.2. Effect of operation temperature

As a representative, SA-ACM-2/PAN was selected to investigate the effect of feed temperature ranging from 313 to 350 K on pervaporation performance with 90 wt% ethanol aqueous solution. It could be seen from Fig. 10(a)–(b) that the separation factor and total flux increased accompanied with the temperature increasing, while the water partial flux increased much faster than ethanol partial flux. This indicated that high temperature was more beneficial to the permeation of water, which resulted in the enhancement of separation factor. According to solution-diffusion mechanism, the molecular transport was controlled by the adsorption process at membrane surface and the diffusion process across membrane bulk. On one hand, the increasing temperature was beneficial to the diffusion of water and ethanol molecule. On the other hand, higher temperature weakened the adsorption of these two components. Due to the effect of hydrogen bond, water molecule had stronger interaction with the hybrid membrane than ethanol molecule, which made ethanol adsorption decrease more

pronouncedly with the increasing temperature [53]. The elevated driving force and molecule diffusion rate with increasing temperature contributed to the enhanced flux [54]. In addition, the temperature dependence of the partial water and ethanol fluxes was measured quantitatively by the apparent activation energy, which could be determined from the Arrhenius equation by

$$J = A_0 \exp\left(-\frac{E_p}{RT}\right)$$

(8)

where J, A_0, E_p, R and T were the permeation flux, pre-exponential factor, apparent activation energy, gas constant, and feed temperature, respectively. As shown in Fig. 10(c), the apparent activation energy of water (E_{pW}) and ethanol (E_{pE}) were 45.7 and 24.5 kJ/mol, respectively. The higher E_{pW} value indicated that water permeation increased faster than ethanol permeation with the increasing temperature [55,56]. And the positive E_{pW} and E_{pE} value indicated that the permeation process of both water and ethanol were dominated by diffusion. Higher temperature loosened the membrane and increased the permeability. However, higher temperature also restricted the adsorption of ethanol molecules on the membrane surface, so that the permeability rate of ethanol increased slower than water.

To eliminate the influence of vapor pressure, driving force of mass transport through the membrane was normalized and the results were shown in Fig. 10(d). With regard to both water and ethanol, the permeant solubility would decrease and permeant diffusivity would enhance when temperature increased. The difference lied in that the enhanced diffusivity of water could compensate the decrease of solubility, while the decreased solubility of ethanol was bigger than the increase of its diffusivity [53]. The weakened coupling effect between water and ethanol restricted ethanol transport along with water molecules [57]. Therefore, higher temperature was beneficial for water permeation, which endowed the hybrid membrane with higher selectivity.

4.3. Effect of feed water concentration

To investigate the effect of feed concentration on SA-ACM-2/PAN membrane performance, the total flux and separation factor at 350 K of feed water concentrations ranging from 5 to 30 wt% were shown in Fig. 11. Fig. 11(a) showed that the separation factor
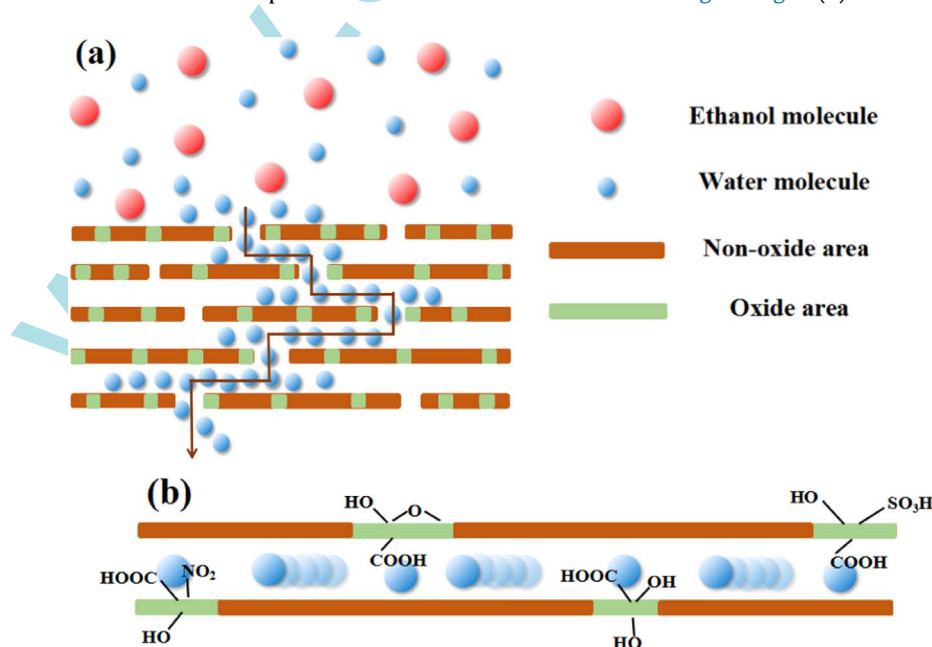

Fig. 9. Schematic representation for selective transport process of water permeation through the ACM nanosheets.

Table 4

Comparison of the pervaporation performance among membranes containing 2D materials.

| Membrane	Alcohol	Feed concentration of water (wt%)	Total flux (g/m² h)	Separation factor	Temperature	Reference
GO/AAO	Butanol	10	3100	230	50	[45]
ZIF-8/PBI	Butanol	15	81	3417	60	[46]
Na$^+$-MMT/CS	Isopropanol	10	142.3	14,992	30	[47]
(GE/GO)/H-PAN	Ethanol	20	2275	304	76	[48]
MFI-type zeolite	Ethanol	5	9800	58	60	[49]
ZIF-90/P84	Isopropanol	15	166	449	60	[50]
GO/PECs	Ethanol	5	268	394	50	[51]
ZIF-8/PI	Ethanol	10	260	300	42	[52]
SA-ACM/PAN	Ethanol	10	1778	1816	76	This study
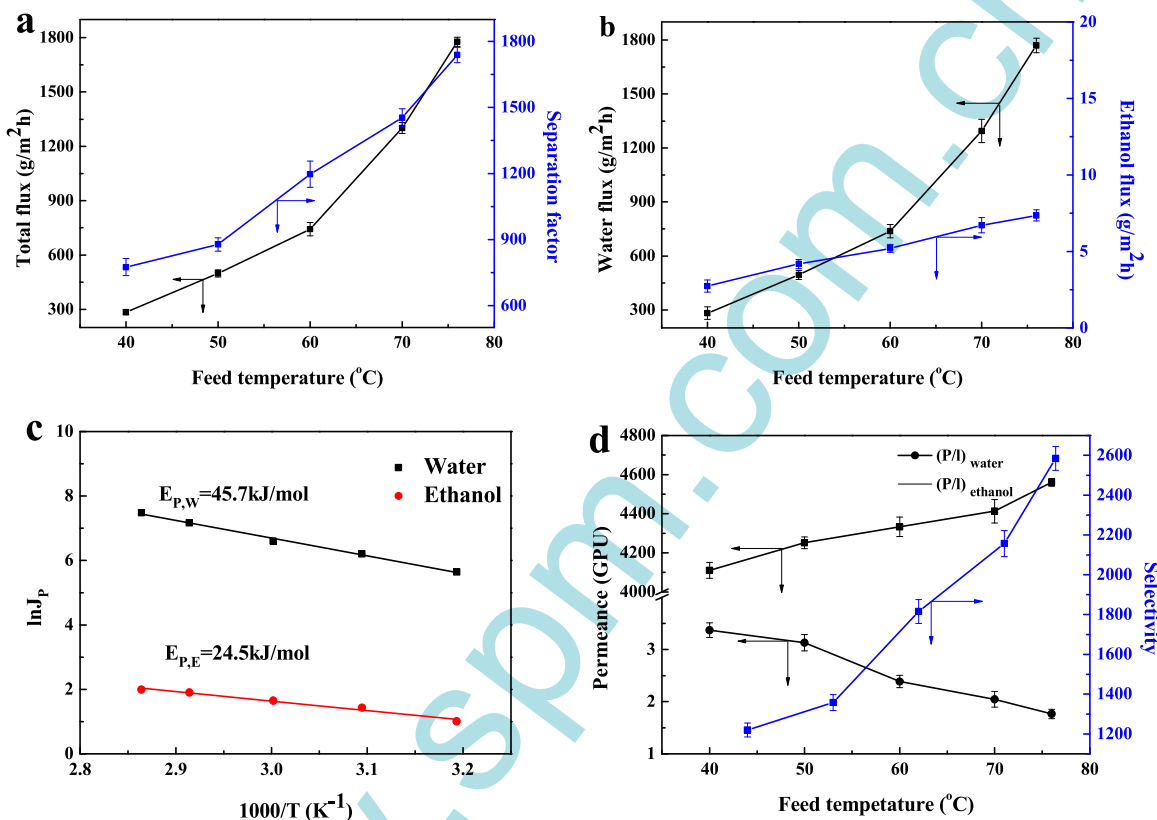
Fig. 10. Effect of feed temperature on separation performance of SA-ACM-2/PAN: (a) total flux and separation factor; (b) water flux and ethanol flux; (c) Arrhenius plots of water and ethanol; (d) water permeance, ethanol permeance and selectivity.

increased first and then decreased as the feed water concentration increased. During the low feed water concentration period, the increasing concentration brought about higher driving force to improve the diffusion of water, which enhanced the selectivity [53]. Then as the concentration increased to a high degree, the influence of membrane swelling surpassed the growing driving force, which led to the decline in selectivity. It also could be seen that the total flux increased continuously with increasing feed water concentration. This might be explained that, the increasing concentration not only resulted in higher membrane swelling, but also led to higher permeant molecules diffusion throughout the membrane, which both enhanced the total flux.

The partial flux of water and ethanol plotted in Fig. 11 (b) displayed the increasing water flux approximately proportional to total flux and general steady ethanol flux, as the concentration increased. Higher water permeations than that of ethanol, was attributed to the small size and strong interaction of water molecules with the membranes. The general steady ethanol flux suggested that the influence of membrane swelling was balanced with the driving force for ethanol permeation. Fig. 11

(c) normalized the membrane thickness and driving force, which further corroborated the swelling effect on the permeation of water and ethanol. As the concentration increased, percolation rate of water and ethanol both increased, while the selectivity first increased and then decreased, which further improved the swelling of the membrane.

4.4. Long-term operation stability

The long-term operation stability of membrane was an important parameter in practical application. The SA-ACM-2/PAN membrane was operated continuously with 90 wt% ethanol aqueous solution at 350 K for over 190 h. Fig. 12 showed that the permeation flux decreased slightly at the beginning and the water content in permeate remained above 99 wt%. Therefore, the membrane exhibited favorable operation stability.

5. Conclusion

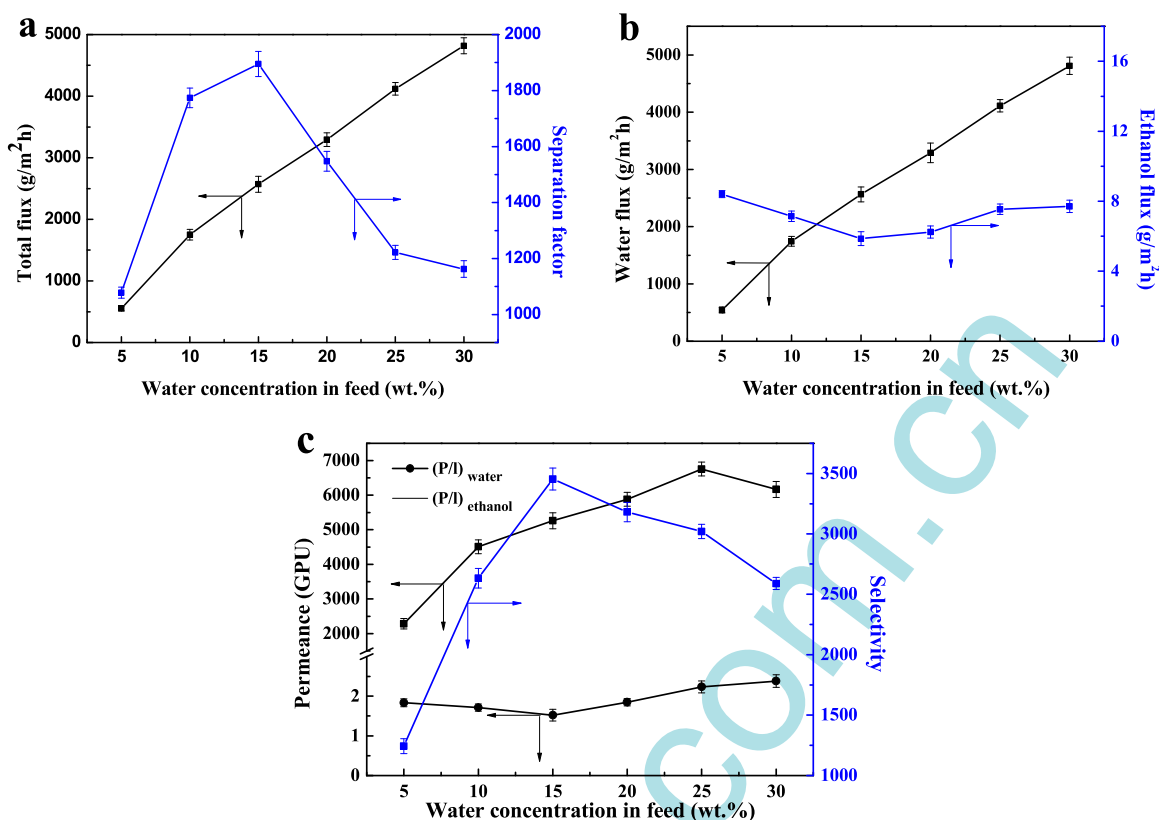In this study, ACM nanosheets were incorporated into SA

Fig. 11. Effect of feed composition on separation performance of SA-ACM-2/PAN: (a) total flux and separation factor; (b) water flux and ethanol flux; (c) water permeance, ethanol permeance and selectivity.
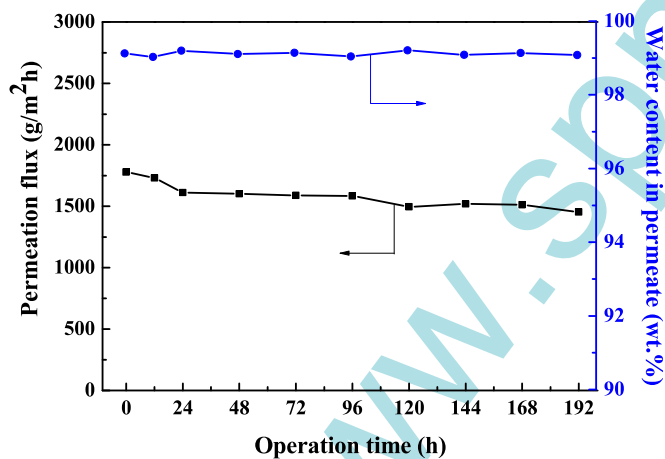

Fig. 12. Long-term separation performance of SA-ACM-2/PAN.

matrix to fabricate hybrid membrane by physical blending method. The amphiphilicity of ACM nanosheets was utilized to intensify adsorption-diffusion process. The hydrophilic region (connected with oxygen-containing functional groups) and hydrophobic region (unoxidized surface) of nanosheets formed water transport channels. The abundant functional groups at the edge of ACM nanosheets preferentially adsorbed water molecules and then allowed water molecules to enter the transport channel due to the hydrogen bond, while the hydrophobic region at the center of ACM nanosheets realized the fast transport of water molecules. Meanwhile, the small nanosheet size with 200–400 nm enhanced the interaction between inorganic filler and polymer to interfere the arrangement of polymer chains more efficiently. The pervaporation experiments manifested that the membrane containing 2 wt% ACM exhibited an optimum performance with permeation

flux of 1778 g/m^2 h (139% of SA control membrane) and separation factor of 1816 (3.06 times of SA control membrane) for 90 wt% ethanol aqueous solution at 350 K. Moreover, the interfacial interactions between ACM nanosheets and SA chains achieved higher swelling resistance, thermal property and mechanical stability of hybrid membranes, which conferred the desirable long-term operation stability. This study may offer a generic and efficient approach utilizing the amphiphilicity of nanosheets to prepare highly water-selective membranes for diverse separation processes.

Acknowledgments

Appendix A. Supporting information

Supplementary data associated with this article can be found in the online version at doi:10.1016/j.memsci.2016.08.049.

Nomenclature

Variables

A	membrane area (m^2)
l	membrane thickness (m)
Q	mass of permeate (g)
t	time interval (h)
SD	Swelling degree (%)
F_E	mass fraction of ethanol in feed solution (wt%)
F_W	mass fraction of water in feed solution (wt%)
P_E	mass fraction of ethanol in permeate solution (wt%)
P_W	mass fraction of water in permeate solution (wt%)
J	permeation flux (g/m^2 h)
J_i	permeation flux of component i (g/m^2 h)
$(P/l)_E$	ethanol permeance (GPU)
$(P/l)_W$	water permeance (GPU)
$(P/l)_i$	the permeance of component i (GPU)
p_{i0}	partial pressures of component i in the feed side (Pa)
p_{il}	partial pressures of component i in the permeate side (Pa)
p_{i0}^{sat}	saturated vapor pressure of pure component i at operation temperature (Pa)
W_D	the mass of dry membrane (g)
W_S	the mass of membrane immersed in the feed mixture (g)
x_{i0}	mole fraction of component i

Greek letters

α	separation factor
β	selectivity
γ_{i0}	activity coefficient of component i
θ	diffraction angle (°)

References

[1] Manish Chhowalla, Hyeon Suk Shin, Goki Eda, The chemistry of two-dimensional layered transition metal dichalcogenide nanosheets, Nat. Chem. 5 (2013) 263–275.

[2] Jonathan N. Coleman, Mustafa Lotya, Arlene O. Neill, Two-dimensional nanosheets produced by liquid exfoliation of layered materials, Sci. 331 (2011) 568–571.

[3] K.S. Novoselov, D. Jiang, F. Schedin, Two-dimensional atomic crystals, PNAS 102 (2005) 10451–10453.

[4] N. Joseph, P. Ahmadiannamini, R. Hoogenboom, Layer-by layer preparation of polyelectrolyte multilayer membranes for separation, Polym. Chem. 5 (2014) 1817–1831.

[5] T.-S. Chung, L.Y. Jiang, Y. Li, Mixed matrix membranes (MMMs) comprising organic polymers with dispersed inorganic fillers for gas separation, Prog. Polym. Sci. 32 (2007) 483–507.

[6] S.P. Dharupaneedi, R.V. Anjanapura, J.M. Han, Functionalized graphene sheets embedded in chitosan nanocomposite membranes for ethanol and isopropanol dehydration via pervaporation, Ind. Eng. Chem. Res. 53 (2014) 14474–14484.

[7] D.P. Suhas, A.V. Raghu, H.M. Jeong, Graphene-loaded sodium alginate nanocomposite membranes with enhanced isopropanol dehydration performance via a pervaporation technique, RSC Adv. 3 (2013) 17120–17130.

[8] J. Zhu, H.N. Zhang, N.A. Kotov, Thermodynamic and structural insights into nanocomposites engineering by comparing two materials assembly techniques for graphene, ACS Nano 7 (2013) 4818–4829.

[9] Y. Shi, S. Jiang, K. Zhou, Influence of g-C3N4 nanosheets on thermal stability and mechanical properties of biopolymer electrolyte nanocomposite films: a novel investigation, ACS Appl. Mater. Interfaces 6 (2014) 429–437.

[10] A.A. Vasileiou, M. Kontopoulou, A. Docoslis, A noncovalent compatibilization approach to improve the filler dispersion and properties of polyethylene/graphene composites, ACS Appl. Mater. Interfaces 6 (2014) 1916–1925.

[11] C. Yang, W.H. Smyrl, E.L. Cussler, Flake alignment in composite coatings, J. Membr. Sci. 231 (2004) 1–12.

[12] Pengzhan Sun, Kunlin Wang, Hongwei Zhu, Recent developments in graphene-based membranes: structure, mass-transport mechanism and potential applications, Adv. Mater. 28 (2016) 2287–2310.

[13] Clement Sanchez, Beatriz Julian, Philippe Belleville, Applications of hybrid organic-inorganic nanocomposites, J. Mater. Chem. 15 (2005) 3559–3592.

[14] H. Li, Z. Song, X. Zhang, Ultrathin, molecular-sieving graphene oxide membranes for selective hydrogen separation, Science 342 (2013) 95–98.

[15] D.R. Dreyer, S. Park, C.W. Bielawski, The chemistry of graphene oxide, Chem. Soc. Rev. 39 (2010) 228–240.

[16] Jing Zhao, Yiwei Zhu, Guangwei He, Incorporating zwitterionic graphene oxides into sodium alginate membrane for efficient water/alcohol separation, ACS Appl. Mater. Interfaces 8 (2016) 2097–2103.

[17] Ji Chen, Yingru Li, Liang Huang, Size fractionation of graphene oxide sheets via filtration through track-etched membranes, Adv. Mater. 27 (2015) 3654–3660.

[18] Xianfu Chen, Gongping Liu, Hanyu Zhang, Fabrication of graphene oxide composite membranes and their application for pervaporation dehydration of butanol, Chin. J. Chem. Eng. 23 (2015) 1102–1109.

[19] M. Fujii, Y. Yamada, T. Imamura, Preparation of aqua-mesophase by nitration or sulfonation of carbonaceous mesophase and properties of carbon material made from it, in: Proceedings of the 18th Biennial Conference of Carbon, 1987, pp. 405–408.

[20] D. Tateishi, K. Esumi, H. Honda, Formation of carbonaceous gel, Carbon 29 (1991) 1296–1298.

[21] Zuojiang Li, Wenfu Yan, Sheng Dai, A novel vesicular carbon synthesized using amphiphilic carbonaceous material and micelle templating approach, Carbon 42 (2004) 767–770.

[22] K. Esumi, S. Eshima, Y. Murakami, Preparation of holly carbon-microbeads from water-in-oil emulsion using amphiphilic carbonaceous material, Colloids Surf. A: Physicochem. Eng. Asp. 108 (1996) 113–116.

[23] Xuefei Guo, Chengyang Wang, Mingming Chen, Carbon coating of Li4Ti5O12 using amphiphilic carbonaceous material for improvement of lithium-ion battery performance, J. Power Sources 214 (2012) 107–112.

[24] Jin Wang, Mingming Chen, Chengyang Wang, Preparation of mesoporous carbons from amphiphilic carbonaceous material for high-performance electric double-layer capacitors, J. Power Sources 196 (2011) 550–558.

[25] L. Ge, W. Zhou, V. Rudolph, Mixed matrix membranes incorporated with size-reduced Cu-BTC for improved gas separation, J. Mater. Chem. A 21 (2013) 6350–6358.

[26] S.D. Bhat, T.M. Aminabhavi, Pervaporation separation using sodium alginate and its modified membranes-a review, Sep. Purif. Rev. 36 (2007) 203–229.

[27] D. Tateishi, K. Esumi, H. Honda, Preparation of carbonaceous gel beads, Carbon 30 (1992) 942–944.

[28] S.J. Tao, Positronium annihilation in molecular substances, J. Chem. Phys. 56 (1972) 5499–5510.

[29] R.W. Baker, J.G. Wijmans, Y. Huang, Permeability, permeance and selectivity: a preferred way of reporting pervaporation performance data, J. Membr. Sci. 348 (2010) 346–352.

[30] E. Shi, W. Huang, Z. Xiao, Influence of binding interface between active and support layers in composite PDMS membranes on permeation performance, J. Appl. Polym. Sci. 104 (2007) 2468–2477.

[31] Boxin Gao, Zhongyi Jiang, Cuihong Zhao, Enhanced pervaporative performance of hybrid membranes containing Fe3O4@CNT nanofillers, J. Membr. Sci. 492 (2015) 230–241.

[32] Y. Zhou, Q. Bao, L.A.L. Tang, Hydrothermal dehydration for the green reduction of exfoliated graphene oxide to graphene and demonstration of tunable optical limiting properties, Chem. Mater. 21 (2009) 2950–2956.

[33] K.N. Kudin, B. Ozbas, H.C. Schniepp, Raman spectra of graphite oxide and functionalized graphene sheets, Nano Lett. 8 (2007) 36–41.

[34] K. Cao, Z. Jiang, J. Zhao, Enhanced water permeation through sodium alginate membranes by incorporating graphene oxides, J. Membr. Sci. 469 (2014) 272–283.

[35] A. Siberberg, Basic principles of colloid science: D. H. Everett, Royal Society of Chemistry, London, 1988. 243 (xv) pp, Journal of Colloid and Interface Science 134 (1990) 593–594.

[36] J. Wang, M.M. Chen, C.Y. Wang, Mesoporous activated carbon from amphiphilic carbonaceous material and its application in EDLC, IEEE INEC 3 (2010) 222–223.

[37] Y.P. Tang, D.R. Paul, T.S. Chung, Free-standing graphene oxide thin films assembled by a pressurized ultrafiltration method for dehydration of ethanol, J. Membr. Sci. 458 (2014) 199–208.

[38] J.T. Chen, Y.J. Fu, Q.F. An, Tuning nanostructure of graphene oxide/polyelectrolyte LbL assemblies by controlling pH of GO suspension to fabricate transparent and super gas barrier films, Nanoscale 5 (2013) 9081–9088.

[39] S. Biniak, G. Szymanski, J. Siedlewski, The characterization of activated carbons with oxygen and nitrogen surface groups, Carbon 35 (1997) 1799–1810.

[40] Q. Zhao, Q.-F. An, T. Liu, Bio-inspired polyelectrolyte complex/graphene oxide nanocomposite membranes with enhanced tensile strength and ultra-low gas permeability, Polym. Chem. 4 (2013) 4298–4302.

[41] J.J. Shieh, R.Y.M. Huang, Chitosan/N-methylol nylon 6 blend membranes for the pervaporation separation of ethanol–water mixtures, J. Membr. Sci. 148 (1998) 243–255.

[42] Dun-Yen Kang, Ho Ming Tong, Ji Zang, Single-walled aluminosilicate nanotube/Poly(vinyl alcohol) nanocomposite membranes, ACS Appl. Mater. Interfaces 4 (2012) 965–976.

[43] J.P. Soares, J.E. Santos, G.O. Chierice, Thermal behavior of alginic acid and its

sodium salt, Eclet. Quim. 29 (2004) 53–56.

[44] Y.-H. Huang, W.-C. Chao, W.-S. Hung, Investigation of fine-structure of poly-amide thin film composite membrane under swelling effect by positron an-nihilation lifetime spectroscopy and molecular dynamics simulation, J. Membr. Sci. 417 (2012) 201–209.

[45] Xianfu Chen, Gongping Liu, Hanyu Zhang, Fabrication of graphene oxide composite membranes and their application for pervaporation dehydration of butanol, Chin. J. Chem. Eng. 23 (2015) 1102–1109.

[46] G.M. Shi, T. Yang, T.S. Chung, Polybenzimidazole (PBI)/zeolitic imidazolate frameworks (ZIF-8) mixed matrix membranes for pervaporation dehydration of alcohols, J. Membr. Sci. 415 (2012) 577–586.

[47] Santosh K. Choudhari, Mahadevappa Y. Kariduraganavar, Development of novel composite membranes using quaternized chitosan and Na$^+$-MMT clay for the pervaporation dehydration of isopropanol, J. Colloid Interface Sci. 338 (2009) 111–120.

[48] Jing Zhao, Yiwei Zhu, Fusheng Pan, Fabricating graphene oxide-based ultrathin hybrid membrane for pervaporation dehydration via layer-by-layer self-as-sembly driven by multiple interactions, J. Membr. Sci. 487 (2015) 162–172.

[49] Shuixin Xia, Yong Peng, Zhengbao Wang, Microstructure manipulation of MFI-type zeolite membranes on hollow fibers for ethanol-water separation, J. Membr. Sci. 498 (2016) 324–335.

[50] D. Hua, Y.K. Ong, Y. Wang, ZIF-90/P84 mixed matrix membranes for perva-poration dehydration of isopropanol, J. Membr. Sci. 453 (2014) 155–167.

[51] Naixin Wang, Shulan Ji, Guojun Zhang, Self-assembly of graphene oxide and polyelectrolyte complex nanohybrid membranes for nanofiltration and per-vaporation, Chem. Eng. J. 213 (2012) 318–329.

[52] Alina Kudasheva, Sara Sorribas, Beatriz Zornoza, Pervaporation of water/ethanol mixtures through polyimide based mixed matrix membranes con-taining ZIF-8, ordered mesoporous silica and ZIF-8-silica core-shell spheres, J. Chem. Technol. Biotechnol. 90 (2015) 669–677.

[53] Steve Yijie Hu, Yufeng Zhang, Darren Lawless, Composite membranes com-prising of polyvinylamine-poly (vinyl alcohol) incorporated with carbon na-notubes for dehydration of ethylene glycol by pervaporation, J. Membr. Sci. 417 (2012) 34–44.

[54] R.Y.M. Huang, R. Pal, G.Y. Moon, Pervaporation dehydration of aqueous ethanol and isopropanol mixtures through alginate/chitosan two ply composite membranes supported by poly(vinylidene fluoride) porous membrane, J. Membr. Sci. 167 (2000) 275–289.

[55] J. Zhao, F. Wang, F.S. Pan, Enhanced pervaporation dehydration performance of ultrathin hybrid membrane by incorporating bioinspired multifunctional modifier and TiCl$_4$ into chitosan, J. Membr. Sci. 446 (2013) 395–404.

[56] C.H. Zhao, H. Wu, X.S. Li, High performance composite membranes with a polycarbophil calcium transition layer for pervaporation dehydration of ethanol, J. Membr. Sci. 429 (2013) 409–417.

[57] R. Jiraratananon, A. Chanachai, R.Y.M. Huang, Pervaporation dehydration of ethanol-water mixtures with chitosan/hydroxyethylcellulose (CS/HEC) com-posite membranes: II. Analysis of mass transport, J. Membr. Sci. 199 (2002) 211–222.